

See discussions, stats, and author profiles for this publication at: <https://www.researchgate.net/publication/264241050>

Expanding the Spectral Tunability of Plasmonic Resonances in Doped Metal–Oxide Nanocrystals through Cooperative Cation–Anion Codoping

ARTICLE in JOURNAL OF THE AMERICAN CHEMICAL SOCIETY · AUGUST 2014

Impact Factor: 12.11 · DOI: 10.1021/ja5039903

CITATIONS

10

READS

122

5 AUTHORS, INCLUDING:



Xingchen Ye

University of California, Berkeley

57 PUBLICATIONS 2,767 CITATIONS

[SEE PROFILE](#)



Taejong Paik

University of Pennsylvania

25 PUBLICATIONS 573 CITATIONS

[SEE PROFILE](#)



Christopher B Murray

University of Pennsylvania

259 PUBLICATIONS 27,581 CITATIONS

[SEE PROFILE](#)

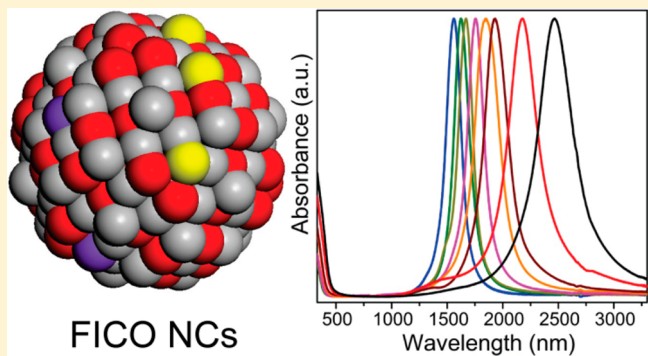
Expanding the Spectral Tunability of Plasmonic Resonances in Doped Metal-Oxide Nanocrystals through Cooperative Cation–Anion Codoping

Xingchen Ye,^{†,§} Jiayang Fei,^{‡,§} Benjamin T. Diroll,[†] Taejong Paik,[†] and Christopher B. Murray*,^{†,‡}

[†]Department of Chemistry and [‡]Department of Materials Science and Engineering, University of Pennsylvania, Philadelphia, Pennsylvania 19104, United States

 Supporting Information

ABSTRACT: We present a generalized cation–anion codoping methodology for the synthesis of monodisperse, doped metal-oxide nanocrystals (NCs) that exhibit near-infrared localized surface plasmon resonance (LSPR) with the highest reported quality factors. We demonstrate that, in addition to the use of common cation dopants, the incorporation of fluorine into the lattice as an anion dopant can further increase the free-carrier concentration within individual NCs; this supports the cooperative effects of mixed cation–anion doping in shifting the LSPR to higher energies. As a result, this method allows the LSPR of doped metal-oxide NCs to become tunable across a significantly broader wavelength range (1.5–3.3 μm), circumventing the prior limitations on the highest possible LSPR energies associated with single-element doping for a given oxide host. The strategy of cation–anion codoping can offer new possibilities for the chemical design of doped semiconductor and metal-oxide NCs with tailored LSPR characteristics.



1. INTRODUCTION

Doping, the process of introducing foreign atoms or impurities into a host lattice, has been widely used for engineering the properties of nanoscale materials in a controlled manner.^{1–7} Many semiconductor and metal-oxide nanocrystals (NCs) can exhibit metallic optical properties in the near-infrared (NIR) and the mid-infrared (MIR) regions when appropriately doped.^{8–14} Unlike conventional plasmonic materials (e.g., Au and Ag) that have a fixed free-electron concentration, the carrier density and thus the absorption features arising from the localized surface plasmon resonance (LSPR) of these emerging plasmonic NCs can be readily tuned by adjusting the doping level. As a result, their unique characteristics are being harnessed for an increasing number of new applications and technologies, such as surface-enhanced infrared absorption (SEIRA),¹⁵ LSPR sensing,¹⁶ smart windows,^{17,18} low-loss optical metamaterials,^{19,20} and bioimaging and therapeutics.^{21,22}

Recently, the tuning of LSPRs at NIR and MIR frequencies has been demonstrated for a wide variety of doped NCs, including metal chalcogenides,^{22–33} phosphides,³⁴ nitrides,³⁵ phosphorus-doped silicon,³⁶ nonstoichiometric oxides,^{37–39} and extrinsically doped oxides.^{17,40–46} For many types of cation-doped plasmonic NCs, it has been observed that, at relatively low doping levels, the LSPR wavelength continuously blue-shifts as the concentration of the cation dopants is increased, which indicates that the majority of dopant atoms are effective in generating free carriers.^{17,40,41,44} However, above a certain dopant concentration, further increases of the doping

level often no longer lead to blue-shifts of the LSPR band, and in some cases red-shifts have been observed.^{40,44,47} These results suggest that at relatively high dopant concentrations, an increasing fraction of the dopant atoms becomes optically inactive. In other words, increasing doping concentrations no longer contributes to increased free carriers in the NCs.

High doping levels in metal-oxide NCs, especially when the dopant concentration approaches the solid–solubility limit in the host lattice, can cause significant distortion of the lattice, which usually results in a loss of control over NC size and shape and the formation of secondary phases.^{41,44} Additionally, the crystal defects that accompany high doping levels often act as trapping centers for free carriers;^{48–50} this limits the ability of the dopant to provide free carriers and thus reduces the carrier concentration. Although the choice of inorganic precursors and ligands can drastically influence the kinetics of precursor decomposition and the doping efficiency, it appears that there exists an upper limit on the accessible carrier densities that result from varying the cation-dopant concentration in almost all extrinsically doped metal-oxide NCs that have been reported; this limit is important because it ultimately determines the highest possible LSPR energy for these NCs. For example, Kanehara et al. reported that the LSPR wavelength of Sn-doped In_2O_3 (ITO) NCs can be tuned from 1.6 to 2.2 μm by changing the Sn-doping level.⁴⁰ Our

Received: April 21, 2014

group recently demonstrated for In-doped CdO (ICO) NCs that the LSPR wavelength is tunable from 1.9 to 3.5 μm depending on the In concentration.⁴⁴ Similar observations have been reported for Al-doped ZnO (AZO) and Ga-doped ZnO (GZO) NCs, for which the shortest LSPR wavelengths are found to be approximately 3 μm .^{41,45} To harness the full potential of these alternative plasmonic NCs, the ability to synthetically tailor the LSPR frequency over a wide spectral range for a given host material is of utmost importance.

Over the past decades, fluorine doping has been extensively utilized to improve the optical quality and the charge-carrier mobility in transparent conducting oxide (TCO) thin films,⁵⁰ such as F-doped SnO₂,^{51,52} F-doped ZnO,⁵³ F- and In-codoped ZnO,⁵⁴ and F-doped CdO.^{55–58} From a theoretical perspective, fluorine doping in TCOs possesses several unique advantages over using cationic metal dopants. First, because the ionic radius of F⁻ (1.33 Å) is slightly smaller than that of O²⁻ (1.40 Å) and the fluorine atom is more electronegative than the oxygen atom,⁵⁹ the substitution of oxygen in the lattice by fluorine can readily occur. Second, according to the classical Drude model, the bulk plasmon frequency is proportional to the square root of the free-electron concentration.²⁴ At high cation-doping levels in various TCOs, it has been observed that scattering by ionized impurity centers and the presence of nonionized defects can limit the highest achievable carrier concentrations.^{17,40,41,44} Alternatively, because a fluorine atom has one more valence electron than an oxygen atom, fluorine atoms can act as electron donors when they replace oxygen atoms. Third, in contrast to the effects of substitutional cation doping, the electronic perturbations induced by fluorine doping are largely localized to the filled valence band, which consists primarily of oxygen atomic orbitals.⁵⁰ As a consequence, impurity scattering and the decrease in the electronic mobility of conduction band electrons can be minimized. Despite these distinct advantages of fluorine doping in TCOs, to our knowledge, the use of fluorine doping to engineer the plasmonic properties of doped metal-oxide NCs remains largely unexplored, and an experimental demonstration of utilizing cation–anion codoping to vary the LSPR energies in doped metal-oxide NCs is still lacking.

In this work, we report for the first time that the simultaneous incorporation of commonly used cation dopants and the anion dopant fluorine can result in advantageous and cooperative effects for increasing the effective carrier concentration and, therefore, can greatly expand the wavelength tunability of LSPRs in doped metal-oxide NCs. The synthesized fluorine- and indium-codoped CdO (FICO) NCs and fluorine- and tin-codoped CdO (FSCO) NCs display remarkably sharp LSPRs that are continuously tunable between 1.5 and 3.3 μm . This method of cation–anion codoping overcomes the difficulty in achieving high LSPR energies that is associated with using a single cation dopant for doped CdO NCs. More generally, this approach offers a promising route to modify the charge-carrier density and thus to expand the LSPR wavelength range in many related doped metal-oxide NC systems.

2. RESULTS AND DISCUSSION

Monodisperse FICO NCs are synthesized by thermal decomposition of cadmium acetylacetone and indium fluoride in a mixture of oleic acid and 1-octadecene at the reflux temperature of the reaction mixture ($\sim 316^\circ\text{C}$). The transmission electron microscopy (TEM) image in Figure 1a shows an example of 17.1 nm FICO NCs synthesized using 5%

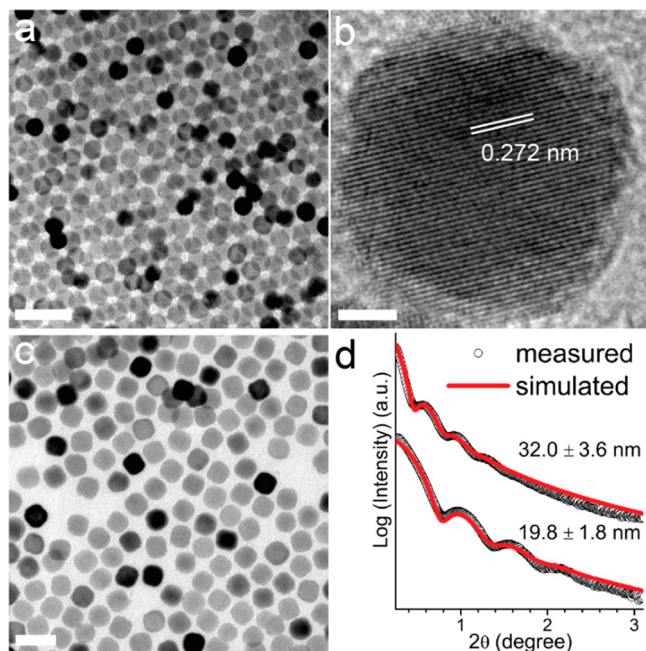


Figure 1. (a) TEM and (b) HRTEM images of 17.1 nm FICO (4.5% In) NCs synthesized with 5% InF₃ and a metal-to-oleic-acid molar ratio (M:OA) of 1:4. (c) TEM image of 28.4 nm FICO (4.3% In) NCs synthesized with 5% InF₃ and M:OA = 1:5. (d) Experimental and simulated SAXS patterns for the FICO NCs shown in (a, b) and (c). Scale bars: (a) 50, (b) 3, and (c) 50 nm.

InF₃. The high-resolution TEM (HRTEM) image in Figure 1b reveals that the FICO NCs are single-crystalline. The lattice fringes with a measured interplanar spacing of 0.272 nm correspond to the {111} planes of the CdO structure. For relatively low InF₃ concentrations (<5%), the size of the FICO NCs can be readily adjusted between 10 and 30 nm by changing the molar ratio between the total metal content and oleic acid in the reaction solution (M:OA). The tunability in NC size becomes limited at higher InF₃ concentrations (>10%, Figure S1). It is also found that increasing the amount of oleic acid while keeping all other synthetic parameters unchanged generally leads to larger NCs (Figures 1c and S1). Figure 1d shows the small-angle X-ray scattering (SAXS) patterns of two differently sized FICO NC samples dispersed in toluene, along with the SAXS patterns simulated for ensembles of spherical particles with an average diameter of 32.0 ± 3.6 and 19.8 ± 1.8 nm, respectively. The SAXS ringing patterns and the excellent fit quality indicate that the FICO NCs are as monodisperse at the ensemble level as they appear in TEM micrographs. The powder X-ray diffraction (XRD) patterns in Figure 2 reveal that the FICO NCs adopt the cubic CdO-type crystal structure. The XRD patterns show no evidence for the presence of secondary phases such as metal fluorides. For FICO NCs synthesized using different percentages of the InF₃ precursor (up to 25%), negligible shifts in the XRD peak positions are observed.

The FICO NCs exhibit an intense and broadly tunable LSPR feature in the NIR region (Figure 3a). Notably, the LSPR peaks for FICO NCs are highly symmetric, which is distinct from those observed in other types of plasmonic metal-oxide NCs, such as ITO and AZO NCs.^{8,17,40,41,46} This could be explained by the screening effect due to the relatively high value of the high-frequency background dielectric constant in CdO.⁶⁰ As shown in Figure 3a, a progressive blue-shift of the LSPR

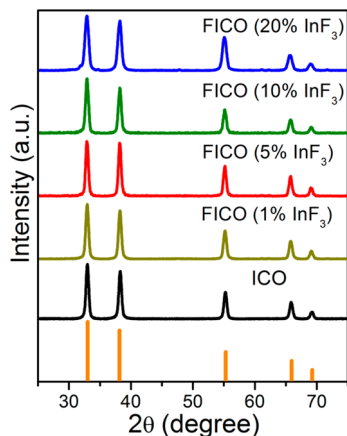


Figure 2. Powder XRD patterns of ICO NCs synthesized using 5% indium acetate and FICO NCs synthesized using various amounts of the InF_3 precursor. The pattern at the bottom (represented as vertical bars) shows the XRD peak positions and the relative intensities of bulk CdO . Each pattern has been normalized to the peak intensity of its strongest peak.

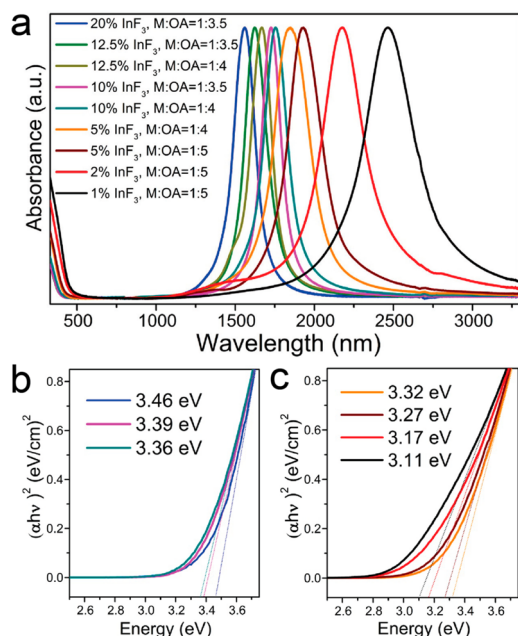


Figure 3. (a) UV-vis-NIR spectra of spherical FICO NCs dispersed in CCl_4 . The percentage of the InF_3 precursor and the metal-to-oleic-acid molar ratios (M:OA) used for NC synthesis are indicated on the graph. (b, c) Plots of $(\alpha h\nu)^2$ vs photon energy (eV) for the FICO NCs shown in (a). The dotted lines represent the fits to the shorter-wavelength linear regions of individual spectra with the x -axis intercepts indicated in the legends.

wavelength is seen as the amount of InF_3 is increased. Importantly, the LSPR wavelength for FICO NCs can be readily tuned from 1.5 to 3.5 μm , which overcomes the difficulty in realizing LSPR wavelengths shorter than 1.9 μm for ICO NCs synthesized using the precursor indium acetate.⁴⁴ Therefore, the use of the metal-fluoride precursor InF_3 allows the simultaneous incorporation of indium and fluorine, both of which are capable of contributing free carriers through aliovalent substitutional doping of the cation and anion sublattices, respectively. The LSPR quality factor for these FICO NCs, defined as the ratio of the LSPR energy to the

plasmon line width, falls in the range of 6.5–12.2 (Table 1), which is the highest reported to date among all semiconductor- and doped-metal-oxide-based plasmonic NCs.^{10,24,27,35,37,40,41,44,46}

Table 1. LSPR Peak Wavelength (λ) and Energy (E), Full Width at Half Maximum (ΔE), and Quality Factor (Q) of LSPR for Spherical FICO NCs

M:OA	initial % In	measured % In ^a	λ (nm)	E (eV)	ΔE (eV)	Q
1:5	1	1.2	2456	0.505	0.078	6.46
1:5	2	1.8	2180	0.569	0.083	6.82
1:5	5	4.3	1928	0.643	0.084	7.67
1:4	5	4.5	1847	0.671	0.094	7.11
1:4	10	7.1	1755	0.707	0.071	9.90
1:3.5	10	8.3	1726	0.718	0.059	12.23
1:4.5	12.5	9.7	1714	0.723	0.067	10.80
1:4	12.5	9.7	1668	0.743	0.069	10.69
1:3.5	12.5	10.8	1622	0.764	0.077	9.87
1:3.5	20	16.5	1560	0.795	0.083	9.63
1:3.5	22.5	18.3	1544	0.803	0.077	10.46

^aMeasured %In: the In content of NCs determined by ICP-OES.

The direct optical bandgap of the FICO NCs can be estimated from the plot of $(\alpha h\nu)^2$ versus $h\nu$ (α : absorption coefficient; $h\nu$: photon energy) by extrapolating the linear portion of the curve to $\alpha = 0$ (Figure 3b,c).^{35,41,44} The monotonic increase in the bandgap energy along with increasing InF_3 doping can be attributed to the Burstein–Moss shift,⁶¹ which is due to the occupation of the low-lying energy levels of the conduction band at high carrier concentrations.

To determine the chemical composition of the FICO NCs, a combination of analytical techniques was employed. The ratio between In and Cd in the NC samples was analyzed by inductively coupled plasma optical emission spectrometry (ICP-OES). As shown in Table 1, the measured In% reflects reasonably well the amount of indium precursor used in NC synthesis. In contrast, the chemical analysis of fluorine can be nontrivial. Using the ion-selective electrode method, it was found that the fluorine content of the FICO NC samples correlates well with the amount of fluorine in the reaction precursors (Table 2). Compositional analysis performed using

Table 2. Fluorine Content of NCs Analyzed Using Ion-Selective Electrode

NC	precursor	% In ^a	λ (nm) ^b	F% ^c	$F/(F + O)\%$ ^d
14 nm FICO spheres	12.5% InF_3	10.8	1622	1.97	13.1
16 nm FICO spheres	2% InF_3	1.8	2180	0.38	2.79
40 nm octahedra	$\text{NaF:Cd} = 0.15$	<0.1	2318	0.55	3.79
16 nm ICO spheres	10% In(ac)_3	7.35	2102	<0.01%	NA

^a% In: the In content (mol %) of NC samples determined by ICP-OES. ^b λ (nm): LSPR peak wavelength. ^cF%: the fluorine content (mass %) of NC samples determined using the ion-selective electrode method. ^d $F/(F + O)\%$: calculated mole fraction of fluorine. The weight percent of NC ligands determined using thermogravimetric analysis is taken into account for the calculation.

energy dispersive X-ray spectroscopy (EDS) also confirms the presence of fluorine in the FICO NCs (Table S1). A decreasing Cd:F atomic ratio is observed for FICO NCs synthesized with increasing amounts of InF_3 .

To gain further insights into the cation–anion codoping and to prove that fluorine is effective in generating free carriers, a series of control experiments were performed. First, when cadmium acetylacetone is decomposed in the presence of a fluoride salt (e.g., LiF , NaF), the resulting CdO NCs can also exhibit a LSPR in the NIR region (Figure S2). These results suggest that fluorine doping itself can sufficiently increase the carrier concentration and thus induce a NIR LSPR for the CdO NCs. They also provide additional evidence that fluorine doping is responsible for increased carrier concentrations as opposed to intrinsic defects in CdO such as oxygen vacancies.⁶² Second, uniform FICO NCs can be synthesized using indium acetate as the indium precursor and LiF as the fluorine source (Figure S3). Here, the use of LiF allows the LSPR energy of the FICO NCs to exceed that of ICO NCs that have a similar indium-doping level. Hence, fluorine doping in CdO NCs and cation doping with indium do not seem to interfere with each other, but rather, they constructively increase the free-carrier concentration beyond what is possible with indium doping alone. Third, various indium-halide precursors were examined for synthesizing doped CdO NCs (Figure 4). InF_3 is far superior to InCl_3 and InBr_3 for synthesizing monodisperse NCs as well as for generating high concentrations of free carriers;

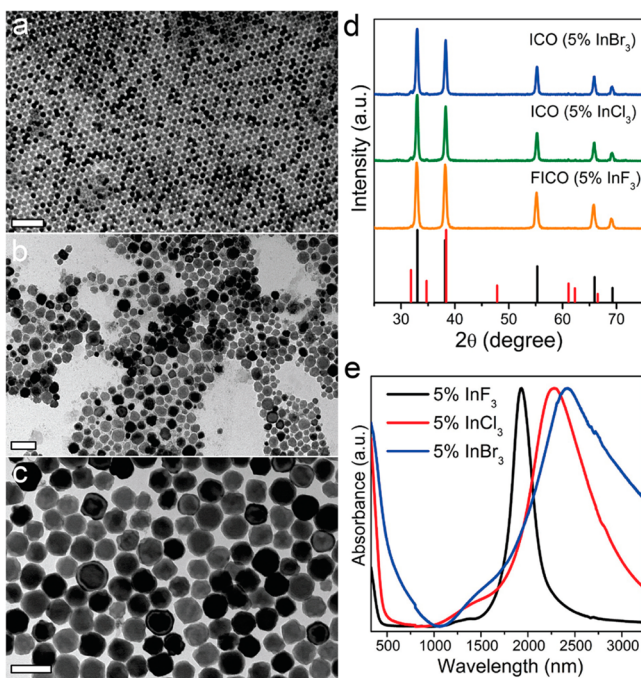


Figure 4. (a–c) TEM images of FICO and ICO NCs synthesized with $\text{M:OA} = 1:4$ and 5% (a) InF_3 , (b) 5% InCl_3 , and (c) 5% InBr_3 , respectively. (d) Powder XRD patterns of FICO and ICO NCs shown in (a–c). The XRD peak positions and the relative intensities corresponding to the bulk CdO (black lines) and the hexagonal-phase Cd (red lines) are shown at the bottom. Each pattern has been normalized to the peak intensity of its strongest peak. (e) UV–vis–NIR spectra of the FICO and ICO NCs shown in (a–c). The actual % In values of the NC samples measured by ICP-OES are 4.3% (for 5% InF_3), 5.8% (for 5% InCl_3), and 5.2% (for 5% InBr_3), respectively. Scale bars: 100 nm.

these elevated carrier concentrations can be ascribed to the easy incorporation of fluorine into the CdO structure due to the similar ionic radii between F^- and O^{2-} . The solution-phase UV–vis–NIR spectra for selected FICO and ICO NCs are shown in Figure 5. The LSPR energies of the FICO NCs are

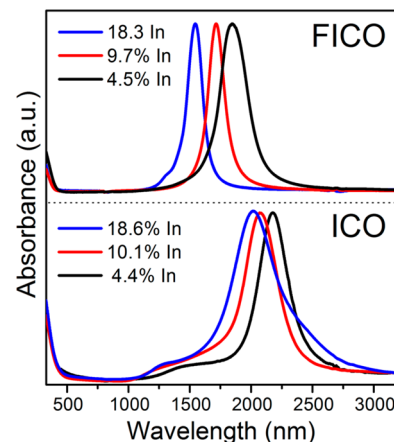


Figure 5. UV–vis–NIR spectra of spherical FICO NCs (top) and ICO NCs (bottom) that have similar In-doping levels (determined by ICP-OES).

consistently higher than those of the ICO NCs that have a nearly identical indium-doping level (measured by ICP-OES). These comparative optical studies of FICO and ICO NCs verify that fluorine doping can produce free carriers in CdO NCs in addition to those generated by indium doping.

Figure 6 presents the dielectric function retrieved from spectroscopic ellipsometry measurements on spin-cast films of

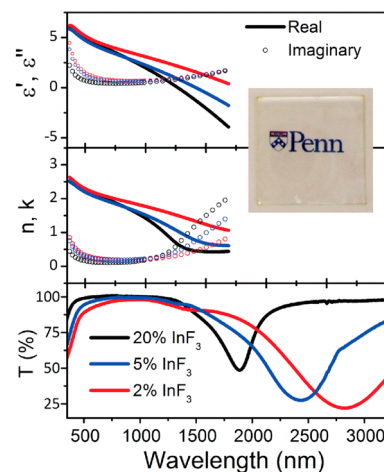


Figure 6. Complex dielectric function (top) and index of refraction (middle) of FICO NCs extracted from thin-film spectroscopic ellipsometry measurements in the spectral region from 370 to 1700 nm. The inset shows a photograph of a spin-cast FICO NC film on a quartz substrate ($2.5 \text{ cm} \times 2.5 \text{ cm} \times 1.6 \text{ mm}$). The experimental transmission spectra of the same NC films used for ellipsometry measurements are shown at the bottom of the figure.

FICO NCs. The inset shows a photograph of a spin-cast FICO NC thin film on a quartz substrate, highlighting the excellent optical quality of the deposited film. The average transmittance in the visible region of the FICO NC thin films is found to be greater than 90%. The oleic-acid-capped FICO NCs in thin

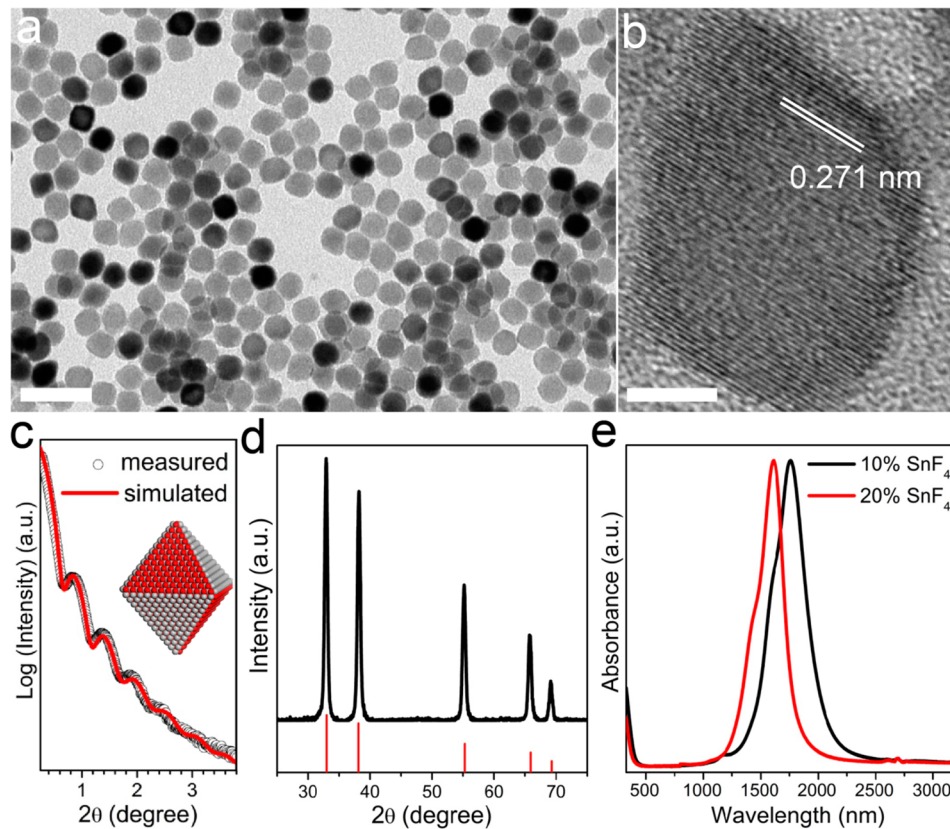


Figure 7. (a) TEM image, (b) HRTEM image, (c) SAXS pattern and (d) powder XRD pattern of F- and Sn-codoped CdO (FSCO) NCs synthesized with 10% SnF_4 . The vertical bars in (d) represent the standard powder XRD pattern of bulk CdO. (e) UV-vis-NIR spectra of FSCO NCs in CCl_4 synthesized using various amounts of the SnF_4 precursor. Scale bars: (a) 50 and (b) 5 nm.

films retain the strong NIR absorption and high visible transmission of the dispersed colloidal NCs. Using the Maxwell–Garnett effective medium approximation, the polarized variable-angle reflectance data for the FICO thin films are fitted to extract the dielectric function of the FICO NCs. Both the dielectric function (ϵ' and ϵ'') and the index of refraction (n and k) are plotted for three FICO samples with various cation–anion doping levels (Figure 6, top and middle), along with the optical transmission of the same films shown at the bottom of Figure 6. A two-oscillator model was developed to account for the two prominent spectral features of the FICO NC films: the bandgap absorption in the blue region of the visible spectrum modeled with a Lorentz oscillator, and the LSPR in the NIR region modeled using a Drude oscillator. The FICO NCs behave as dielectrics in the visible region ($\epsilon' > 0$), but concomitant with the strong LSPR feature, the real part of the complex dielectric function ϵ' crosses zero at 1269 and 1417 nm for FICO NCs synthesized using 20% and 5% InF_3 , respectively. At lower frequencies, ϵ' becomes negative, a signature of a metallic response. These features are observed in all FICO NC films measured (Figure 6) and are similar to those previously reported for ICO NC films.⁴⁴ The crossover frequency, defined as the frequency at which ϵ' crosses zero, blue-shifts with increasing amounts of the InF_3 precursor, which indicates increasing carrier concentrations at higher doping levels (Figure 6, top). It is worth noting that the crossover frequencies for the FICO NCs are generally higher than those of the ICO NCs,⁴⁴ which also suggests higher carrier concentrations resulting from the fluorine doping.

To explore the generality of the cation–anion codoping strategy for the synthesis of doped plasmonic metal-oxide NCs, we have also synthesized F- and Sn-codoped CdO (FSCO) NCs using cadmium acetylacetone and tin(IV) fluoride as the precursors. As shown in Figures 7a and S5, monodisperse octahedral FSCO NCs can be synthesized under conditions similar to those for FICO NCs. The size uniformity of the FSCO NCs is further manifested in the experimental SAXS pattern, which is in excellent agreement with the simulated scattering pattern for an ensemble of octahedral-shaped particles that have an average size (tip-to-tip length) of 27.0 ± 2.0 nm (Figure 7c). The FSCO NCs are generally more faceted and elongated than the FICO NCs. The HRTEM image of a single FSCO NC reveals an interplanar distance of 0.271 nm, which is consistent with the lattice spacing of the $\{111\}$ planes of the CdO structure (Figure 7b). The phase purity of the FSCO NCs is further confirmed by the powder XRD pattern (Figure 7d). No other oxide phases, including tin oxides and cadmium stannates, are found under the synthetic conditions that have been explored (<20% SnF_4). A strong LSPR is also observed for FSCO NCs in the NIR range (Figure 7e). The LSPR wavelength blue-shifts with increasing amounts of the SnF_4 precursor, indicative of higher carrier concentrations as a result of higher levels of tin and fluorine dopants. Similar to the results discussed above for FICO and ICO NCs, the LSPR energies of FSCO NCs are found to be much higher than those of Sn-doped CdO (SCO) NCs with a similar Sn-doping level (Figure S7). Interestingly, the absorption spectra of FSCO NCs typically show a small shoulder at energies higher than the main LSPR peak (Figure 7e), which might be

related to the octahedral shape of the FSCO NCs, as similar spectral features are not observed in the case of spherical FICO NCs presented above. It is worth mentioning that shape-dependent LSPR properties of doped metal-oxide NCs have been reported for plasmonic ICO and Cs_xWO_3 NCs.^{39,44} Moreover, it is unlikely that higher-order plasmonic resonances can play a significant role, given the typical sizes of the FSCO NCs (~ 20 nm) and the wavelengths of interest (1500–2500 nm).

3. CONCLUSIONS

In summary, we have described a generalized cation–anion codoping methodology for the synthesis of monodisperse, plasmonic, doped metal-oxide NCs. We demonstrate that the incorporation of the anion dopant fluorine into a host lattice, in addition to the use of common cation dopants, can further raise the free carrier concentration within individual NCs, indicating the cooperative roles of cation–anion codoping that shift the NC LSPR toward higher energies. As a result, this method circumvents the prior limitations on the highest achievable LSPR frequencies associated with changing only the concentrations of substitutional cation dopants for a given oxide host; as a result, it allows the LSPR of doped metal-oxide NCs to be tunable across a significantly broader wavelength range. Using FICO and FSCO NCs as two examples, we show that the LSPR wavelength of the NCs can be continuously adjusted between 1.5 and $3.3\ \mu\text{m}$, enabling high-quality plasmonic NC building blocks for a broad wavelength range including the telecommunication wavelength ($\lambda = 1.55\ \mu\text{m}$). The FICO NCs exhibit the highest LSPR quality factor reported so far for NIR plasmonic semiconductor and doped metal-oxide NCs, making them ideally suited for applications that rely on local-field enhancement. The observed bandgap widening (shifts in the absorption edge to higher energies) with increasing doping levels can be attributed to the increase in the carrier concentration. Spectroscopic ellipsometry characterization of FICO NC thin films reveals negative values for the real part of the dielectric function in the NIR region, along with a small imaginary part, signifying a high oscillator strength and low intrinsic optical losses for the LSPR of FICO NCs. Altogether, our work opens up new possibilities for the chemical design and discovery of doped semiconductor and metal-oxide NCs with tailored LSPRs in the NIR region.

■ ASSOCIATED CONTENT

Supporting Information

Experimental details; additional TEM images of FICO NCs synthesized under various conditions; TEM images of F-doped CdO NCs and doped CdO NCs synthesized with various metal halide precursors; absorption spectra of FICO NCs dispersed in three different solvents; additional TEM and SEM images of FSCO NCs synthesized under various conditions; table summarizing the doping level, LSPR energy and quality factors of FICO NCs; table of elemental analysis results for FICO NCs. This material is available free of charge via the Internet at <http://pubs.acs.org>.

■ AUTHOR INFORMATION

Corresponding Author

cbmurray@sas.upenn.edu

Author Contributions

[§]These authors contributed equally to this work.

Notes

The authors declare no competing financial interest.

■ ACKNOWLEDGMENTS

This work received primary support for the development of the synthesis and optical characterization from the Office of Naval Research Multidisciplinary University Research Initiative on optical metamaterials through award N00014-10-1-0942. Partial support from the U.S. Department of Energy Office of Basic Energy Sciences, Division of Materials Science and Engineering, under award no. DE-SC0002158 enabled the X-ray analysis including SAXS studies. C.B.M. is also grateful to the Richard Perry University Professorship for support of his supervisor role. We thank Danielle Reifsnyder Hickey for useful discussions. We also thank Dr. Douglas Yates and Dr. Jamie Ford at the Penn Regional Nanotechnology Facility for support on electron microscopy, Dr. Paul Heiney for assistance with SAXS measurements, and Dr. David Vann for support with ICP-OES measurements.

■ REFERENCES

- (1) Alivisatos, A. P. *Science* **1996**, *271*, 933–937.
- (2) Norris, D. J.; Yao, N.; Charnock, F. T.; Kennedy, T. A. *Nano Lett.* **2000**, *1*, 3–7.
- (3) Radovanovic, P. V.; Gamelin, D. R. *J. Am. Chem. Soc.* **2001**, *123*, 12207–12214.
- (4) Stowell, C. A.; Wiacek, R. J.; Saunders, A. E.; Korgel, B. A. *Nano Lett.* **2003**, *3*, 1441–1447.
- (5) Norris, D. J.; Efros, A. L.; Erwin, S. C. *Science* **2008**, *319*, 1776–1779.
- (6) Wang, F.; Han, Y.; Lim, C. S.; Lu, Y. H.; Wang, J.; Xu, J.; Chen, H. Y.; Zhang, C.; Hong, M. H.; Liu, X. G. *Nature* **2010**, *463*, 1061–1065.
- (7) Mocatta, D.; Cohen, G.; Schattner, J.; Millo, O.; Rabani, E.; Banin, U. *Science* **2011**, *332*, 77–81.
- (8) Mendelsberg, R. J.; Garcia, G.; Li, H.; Manna, L.; Milliron, D. J. *J. Phys. Chem. C* **2012**, *116*, 12226–12231.
- (9) Scotognella, F.; Valle, G.; Srimath Kandada, A. R.; Zavelani-Rossi, M.; Longhi, S.; Lanzani, G.; Tassone, F. *Eur. Phys. J. B* **2013**, *86*, 154.
- (10) Comin, A.; Manna, L. *Chem. Soc. Rev.* **2014**, *43*, 3957–3975.
- (11) Liu, X.; Swihart, M. T. *Chem. Soc. Rev.* **2014**, *43*, 3908–3920.
- (12) Faucheaux, J. A.; Stanton, A. L. D.; Jain, P. K. *J. Phys. Chem. Lett.* **2014**, *5*, 976–985.
- (13) Lounis, S. D.; Runnerstrom, E. L.; Llordés, A.; Milliron, D. J. *J. Phys. Chem. Lett.* **2014**, *5*, 1564–1574.
- (14) Ye, X.; Hickey, D. R.; Fei, J.; Diroll, B. T.; Paik, T.; Chen, J.; Murray, C. B. *J. Am. Chem. Soc.* **2014**, *136*, 5106–5115.
- (15) Abb, M.; Wang, Y.; Papasimakis, N.; de Groot, C. H.; Muskens, O. L. *Nano Lett.* **2013**, *14*, 346–352.
- (16) Ohodnicki, P. R.; Wang, C.; Andio, M. *Thin Solid Films* **2013**, *539*, 327–336.
- (17) Garcia, G.; Buonsanti, R.; Runnerstrom, E. L.; Mendelsberg, R. J.; Llordés, A.; Anders, A.; Richardson, T. J.; Milliron, D. J. *Nano Lett.* **2011**, *11*, 4415–4420.
- (18) Llordés, A.; Garcia, G.; Gazquez, J.; Milliron, D. J. *Nature* **2013**, *500*, 323–326.
- (19) Boltasseva, A.; Atwater, H. A. *Science* **2011**, *331*, 290–291.
- (20) Naik, G. V.; Liu, J.; Kildishev, A. V.; Shalaev, V. M.; Boltasseva, A. *Proc. Natl. Acad. Sci. U.S.A.* **2012**, *109*, 8834–8838.
- (21) Hessel, C. M.; Pattani, V. P.; Rasch, M.; Panthani, M. G.; Koo, B.; Tunnell, J. W.; Korgel, B. A. *Nano Lett.* **2011**, *11*, 2560–2566.
- (22) Liu, X.; Lee, C.; Law, W.-C.; Zhu, D.; Liu, M.; Jeon, M.; Kim, J.; Prasad, P. N.; Kim, C.; Swihart, M. T. *Nano Lett.* **2013**, *13*, 4333–4339.
- (23) Zhao, Y.; Pan, H.; Lou, Y.; Qiu, X.; Zhu, J.; Burda, C. *J. Am. Chem. Soc.* **2009**, *131*, 4253–4261.

- (24) Luther, J. M.; Jain, P. K.; Ewers, T.; Alivisatos, A. P. *Nat. Mater.* **2011**, *10*, 361–366.
- (25) Dorfs, D.; Härtling, T.; Miszta, K.; Bigall, N. C.; Kim, M. R.; Genovese, A.; Falqui, A.; Povia, M.; Manna, L. *J. Am. Chem. Soc.* **2011**, *133*, 11175–11180.
- (26) Hsu, S.-W.; On, K.; Tao, A. R. *J. Am. Chem. Soc.* **2011**, *133*, 19072–19075.
- (27) Kriegel, I.; Jiang, C.; Rodríguez-Fernández, J.; Schaller, R. D.; Talapin, D. V.; Da Como, E.; Feldmann, J. *J. Am. Chem. Soc.* **2012**, *134*, 1583–1590.
- (28) Xie, Y.; Riedinger, A.; Prato, M.; Casu, A.; Genovese, A.; Guardia, P.; Sottini, S.; Sangregorio, C.; Miszta, K.; Ghosh, S.; Pellegrino, T.; Manna, L. *J. Am. Chem. Soc.* **2013**, *135*, 17630–17637.
- (29) Kriegel, I.; Rodríguez-Fernández, J.; Wisnet, A.; Zhang, H.; Waurisch, C.; Eychmüller, A.; Dubavik, A.; Govorov, A. O.; Feldmann, J. *ACS Nano* **2013**, *7*, 4367–4377.
- (30) Xie, Y.; Carbone, L.; Nobile, C.; Grillo, V.; D’Agostino, S.; Della Sala, F.; Giannini, C.; Altamura, D.; Oelsner, C.; Kryschi, C.; Cozzoli, P. D. *ACS Nano* **2013**, *7*, 7352–7369.
- (31) Li, W.; Zamani, R.; Rivera Gil, P.; Pelaz, B.; Ibáñez, M.; Cadavid, D.; Shavel, A.; Alvarez-Puebla, R. A.; Parak, W. J.; Arbiol, J.; Cabot, A. *J. Am. Chem. Soc.* **2013**, *135*, 7098–7101.
- (32) Liu, X.; Wang, X.; Swihart, M. T. *Chem. Mater.* **2013**, *25*, 4402–4408.
- (33) Hsu, S.-W.; Ngo, C.; Tao, A. R. *Nano Lett.* **2014**, *14*, 2372–2380.
- (34) Manna, G.; Bose, R.; Pradhan, N. *Angew. Chem. Int. Ed.* **2013**, *52*, 6762–6766.
- (35) Palomaki, P. K. B.; Miller, E. M.; Neale, N. R. *J. Am. Chem. Soc.* **2013**, *135*, 14142–14150.
- (36) Rowe, D. J.; Jeong, J. S.; Mkhdyan, K. A.; Kortshagen, U. R. *Nano Lett.* **2013**, *13*, 1317–1322.
- (37) Manthiram, K.; Alivisatos, A. P. *J. Am. Chem. Soc.* **2012**, *134*, 3995–3998.
- (38) Huang, Q.; Hu, S.; Zhuang, J.; Wang, X. *Chem.—Eur. J.* **2012**, *18*, 15283–15287.
- (39) Mattox, T. M.; Bergerud, A.; Agrawal, A.; Milliron, D. J. *Chem. Mater.* **2014**, *26*, 1779–1784.
- (40) Kanehara, M.; Koike, H.; Yoshinaga, T.; Teranishi, T. *J. Am. Chem. Soc.* **2009**, *131*, 17736–17737.
- (41) Buonsanti, R.; Llordes, A.; Aloni, S.; Helms, B. A.; Milliron, D. J. *Nano Lett.* **2011**, *11*, 4706–4710.
- (42) Lee, J.; Lee, S.; Li, G.; Petruska, M. A.; Paine, D. C.; Sun, S. J. *Am. Chem. Soc.* **2012**, *134*, 13410–13414.
- (43) Trizio, L. D.; Schimpf, A. M.; Llordes, A.; Gamelin, D. R.; Simonutti, R.; Milliron, D. J. *Chem. Mater.* **2013**, *25*, 3383–3390.
- (44) Gordon, T. R.; Paik, T.; Klein, D. R.; Naik, G. V.; Caglayan, H.; Boltasseva, A.; Murray, C. B. *Nano Lett.* **2013**, *13*, 2857–2863.
- (45) Della Gaspera, E.; Bersani, M.; Cittadini, M.; Guglielmi, M.; Pagani, D.; Noriega, R.; Mehra, S.; Salleo, A.; Martucci, A. *J. Am. Chem. Soc.* **2013**, *135*, 3439–3448.
- (46) Lounis, S. D.; Runnerstrom, E. L.; Bergerud, A.; Nordlund, D.; Milliron, D. J. *J. Am. Chem. Soc.* **2014**, *136*, 7110–7116.
- (47) Hudait, M. K.; Modak, P.; Krupanidhi, S. B. *Mater. Sci. Eng., B* **1999**, *60*, 1–11.
- (48) Lee, H.-C.; Park, O. O. *Vacuum* **2004**, *75*, 275–282.
- (49) Liu, B.; Gu, M.; Liu, X.; Huang, S.; Ni, C. *Appl. Phys. Lett.* **2010**, *97*, 122101.
- (50) Gordon, R. G. *MRS Bull.* **2000**, *25*, 52–57.
- (51) Dominici, L.; Michelotti, F.; Brown, T. M.; Reale, A.; Di Carlo, A. *Opt. Express* **2009**, *17*, 10155–10167.
- (52) Nadarajah, A.; Carnes, M. E.; Kast, M. G.; Johnson, D. W.; Boettcher, S. W. *Chem. Mater.* **2013**, *25*, 4080–4087.
- (53) Choi, Y.-J.; Park, H.-H. *J. Mater. Chem. C* **2014**, *2*, 98–108.
- (54) Seo, J.-S.; Jeon, J.-H.; Hwang, Y. H.; Park, H.; Ryu, M.; Park, S.-H. K.; Bae, B.-S. *Sci. Rep.* **2013**, *3*, 2085.
- (55) Ferro, R.; Rodríguez, J. A. *Thin Solid Films* **1999**, *347*, 295–298.
- (56) Ferro, R.; Rodríguez, J. A. *Sol. Energy Mater. Sol. Cells* **2000**, *64*, 363–370.
- (57) Santos-Cruz, J.; Torres-Delgado, G.; Castanedo-Perez, R.; Zúñiga-Romero, C. I.; Zelaya-Angel, O. *Thin Solid Films* **2007**, *515*, 5381–5385.
- (58) Deokate, R. J.; Pawar, S. M.; Moholkar, A. V.; Sawant, V. S.; Pawar, C. A.; Bhosale, C. H.; Rajpure, K. Y. *Appl. Surf. Sci.* **2008**, *254*, 2187–2195.
- (59) Shannon, R. D. *Acta Crystallogr., Sect. A* **1976**, *32*, 751–767.
- (60) Mendelsberg, R. J.; Zhu, Y.; Anders, A. *J. Phys. D: Appl. Phys.* **2012**, *45*, 425302.
- (61) Burstein, E. *Phys. Rev.* **1954**, *93*, 632–633.
- (62) Burbano, M.; Scanlon, D. O.; Watson, G. W. *J. Am. Chem. Soc.* **2011**, *133*, 15065–15072.